LiNi$_{0.8}$Co$_{0.1}$Mn$_{0.1}$O$_2$/Li$_x$CoO$_2$ hybrid cathode and Its Enhanced Electrochemical Properties for Lithium Ion Batteries

Li-Zhen Wang[*], *Jian-Hui Zhang, Hua Fang, Ke-Zheng Gao, Ji Yan*[**]

School of Materials and Chemical Engineering, Zhengzhou University of Light Industry, Zhengzhou, Henan, 450001, PR China
[*]E-mail: wlz@zzuli.edu.cn and jiyan@zzuli.edu.cn

In this study, core-shell like LiNi$_{0.8}$Co$_{0.1}$Mn$_{0.1}$O$_2$@Li$_x$CoO$_2$ hybrid cathode has been synthesized by an improved liquid method. The physical and chemical properties of the hybrid material have been characterized through XRD, SEM, TEM, XPS and related electrochemical approaches. An interesting pheonmenon is observed that Li$_x$CoO$_2$ can be effectively coated not only on the surface of LiNi$_{0.8}$Co$_{0.1}$Mn$_{0.1}$O$_2$ aggregation but also filled into the primary particle gap without altering the layer crystal structure of LiNi$_{0.8}$Co$_{0.1}$Mn$_{0.1}$O$_2$. The unique coating layer can effectively alleviate the corrosion of electroactive material from electrolyte through impeding the direct contact of hydrogen fluoride. Moreover, the shielding effect of Li$_x$CoO$_2$ layer can also hamper the attack from OH$^-$ and CO$_2$ formed during material storage and prevent the formation of solid electrolyte interface film on the surface of primary LiNi$_{0.8}$Co$_{0.1}$Mn$_{0.1}$O$_2$ during charge/discharge cycling. Benefiting from above aspects, the achieved hybrid material exhibits superior cycling stability and high-rate capability, demonstrating a promising value in commercial lithium ion batteries.

1. INTRODUCTION

Nickel-rich material has commonly been recognized as a promising cathode for next-generation high-power lithium ion batteries. Its aggregation-like structure ranges from 1-3 μm to 10-20 μm, which is composed of primary particles with several hundred nano-size and is very useful to achieve high tap-density for commerial application. The inner architecture of the aggregation is compact with the crystal boundary or space gap exists as well[1-4]. However, nickel-rich material also suffers from fast capacity decay and poor rate capability. It has been proven that the crack of aggregation framework from strong structure shrinkage during the extraction/insertion of lithium ion takes responsible for the capacity decay

and poor electrochemical rate performance[5]. Although the cracked particles may increase the surface area of electroactive material, the increased contact ratio between the electroactive particle and HF in electrolyte also results in more severe side-reaction[6-8], thus leading to the fading of electrochemical properties. Simultaneously, the cracked particle reduces the effective binding between electroactive material, conductive carbon and binder, which is harmful to the cycling life of batteries as well[9].

As we known, surface coating technology has widely been adopted to improve the drawbacks of cathode material. Up to now, a lot of strategies including sol-gel method[10,11], solve-thermal method[12], and atomic layer deposition method[13,14] have been adopted for coating other materials on nickel-rich materials to achieve improved electrochemical performances. However, the as-prepared materials based on above mentioned methods always surface from some disadvantages such as huge coating particle, low surface coating efficiency, and difficulty penetration into the inner of aggregation structure. In spite of hindering the direct contact between electroactive material and hydrogen fluoride in electrolyte, the crack issue cannot be efficiently improved and the cycling life of Ni-rich cathode materials is still un-satisfy[15, 16]. In addition, the residual Li-containing composite on surface of Nickel-rich cathode could arise a series parasitic reactions[17,18], the strategy to improve the cycling stability and rate performance of Ni-rich cathode material still needs further investigation.

In this article, an improved liquid strategy has been introduced to not only coating Li_xCoO_2 on the surface of $LiNi_{0.8}Co_{0.1}Mn_{0.1}O_2$ cathode aggregation but also filling Li_xCoO_2 on the inner gap space between primary $LiNi_{0.8}Co_{0.1}Mn_{0.1}O_2$ particles. The crystal structure, surface morphology, element valance as well as electrochemical behavior of $LiNi_{0.8}Co_{0.1}Mn_{0.1}O_2$ material before/after Li_xCoO_2 coating have been investigated. With respecting the improved cycling stability and rate performance, the proposed strategy and research viewpoint can be extended to investigate other hybrid cathode materials in lithium ion batteries.

2. EXPERIMENTAL

2.1. Materials synthesis

All chemicals used in experiment were directly purchased from Sigma-Aldrich and used without further purification. All hybrid cathode materials were prepared as following procedure. Briefly, 5 mmol CH_3COOLi and 5 mmol $(CH_3COO)_2Co$ were dissolved into 30 ml mixture solution (15 ml H_2O+15 ml EtOH) under continuous stirring until an uniform pink solution was formed. Then, 1 g of $LiNi_{0.8}Co_{0.1}Mn_{0.1}O_2$ was added and stirred for another 12 h. The obtained suspension was heated at 60 °C water bath until a slurry formed. The slurry was further dried at 100 °C in a vacuum oven for 12 h. Finally, all the prepared precursors were annealed at 600 °C for 5 h in air at a ramping rate of 5 °C min^{-1} to achieve final products. Herein, for convenience, the $LiNi_{0.8}Co_{0.1}Mn_{0.1}O_2$ coated with 0 wt%, 1 wt%, 2 wt% and 3 wt% of $LiCoO_2$ can be denoted as NCM, NCM-LCO-1, NCM-LCO-2 and NCM-LCO-3, respectively.

2.2. Materials characterization

The crystal structure and morphology of the prepared composites were analyzed by using X-ray diffraction (XRD, Philips PC-APD with Cu Ka radiation), field-emission gun scanning electron microscope (SEM, Hitachi S-4800) and high resolution transmission electron microscope (HRTEM, JEM-1010, JEOL). Fourier transform infrared spectroscopy (FTIR, Nicolet iS5) was applied to check the surface chemical functional groups. X-ray photoelectron spectroscopy (XPS, Thermo Fisher ESCALAB 250 Xi XPS instrument) was conducted to study the surface oxidation status and element valence of the composites. The Barrett-Emmett-Teller (BET) method was used to evaluate the surface area and pore size distribution of the samples (N_2 adsorption analyses, BELSORP-mini II, Japan) at 77 K.

2.3. Electrochemical test and results.

For working electrode, the as-prepared hybrid composite (80 wt%) was mixed with super P (10 wt%) and poly(vinyldifluoride) (PVDF) (10 wt%) by using N-methyl-2-pyrrolidone (NMP) as dispersant. The formed slurry was pasted onto an aluminum foil and dried at 120 °C for 12 h in a vacuum oven. Then, 2016-type coin cell was assembled using the obtained hybrid electrode as cathode, lithium metal as anode and 1 M $LiPF_6$ in ethylene carbonate/dimethyl carbonate/diethyl carbonate (1:1:1v/v/v) as electrolyte. The assembling atmosphere is controlled by an argon-filled glove box (Maxbrunn, Germany) with controlling H_2O and O_2 levels less than 0.5 ppm. The mass loading of active material was determined to be around 2.0-3.0 mg cm^{-2}. The assembled coin cell was galvanostatically charged and discharged between 2.7 and 4.5 V by applying 0.1 C, 0.2 C, 0.5 C, 1 C and 2 C rate on NEWARE BTS-610 at room temperature (Here, 1 C corresponds to 275 mA g^{-1}). Cyclic voltammetry (CV) tests were recorded with an electrochemical workstation (CHI 660E, CHENHUA) between 2.7 and 4.5 V at a scan rate of 0.1 mV s^{-1}. Electrochemical impedance spectra (EIS) measurements were performed using another electrochemical workstation (Gamry Instrument model PCI 4-750, USA) in a frequency range from 100.0 KHz to 0.01 Hz in a potential interval of 5 mV. To investigate the morphological and crystal alteration before/after charge & discharge cycling, the electrode was disassembled in the glove-box and washed by dimethyl carbonate for three times, followed drying in a vacuum oven at 60 °C for 12 h.

3. RESULTS AND DISCUSSION

Figure 1 gives the XRD pattern of all samples. The results indicate that the crystal structure belongs to α-$NaFeO_2$ with a space group of R3m, which keeps consistent with the diffraction peaks of NCM[19], demonstrating no alteration of $LiNi_{0.8}Co_{0.1}Mn_{0.1}O_2$ crystal structure after Li_xCoO_2 coating. The detail crystal parameters of all samples are listed in Table 1. In comparison with NCM, the 2θ value reduces with the increase of *d* value after coating Li_xCoO_2. Moreover, the depressed *a* axis and the expanded *c* axis are detected with increasing the ratio of Li_xCoO_2. The large *c* axis is generally related with the fast Li-ion diffusion. The increased crystal volume has also been detected, which is mainly because of the bigger ionic size of Li^+ (0.076nm) than that of Ni^{2+}(0.069 nm), Co^{2+}(0.0545 nm) or

Mn^{4+}(0.053 nm)[20]. In addition, the relative ratio of $I_{(003)}/I_{(104)}$ and c/a reaches the maximum value after coating 2 wt% of Li_xCoO_2, suggesting the excellent stability of layer-structure and lower cation-random mixing extent for the as-obtained hybrid material.

Figure 2a-f show the SEM images of NCM, NCM-LCO-1, NCM-LCO-2 and NCM-LCO-3 samples. As observed, the NCM is of sphere secondary particle and composed of primary particles in nanosize. The surface is relatively smooth and the primary particle keeps sphere-type geometric morphology as well. After coating with 1wt% Li_xCoO_2, the surface of $LiNi_{0.8}Co_{0.1}Mn_{0.1}O_2$ particle becomes rough and its surface is uniformly coated by some tiny particles. When 2 wt% Li_xCoO_2 is introduced, it is observed that the coating material has been transformed into "drop" prototype on the surface of $LiNi_{0.8}Co_{0.1}Mn_{0.1}O_2$ and into the gap between the primary particles. With the coating ratio reaches 3 wt%, the coating material acts like glue on the surface of $LiNi_{0.8}Co_{0.1}Mn_{0.1}O_2$ particle to bridge the primary particles together and result in the formation of fuzzy surface. The surface coating layer becomes so thick that the boundary of primary particle becomes indistinct. The morphology transformation illustrates the successful assembling of core-shell like $LiNi_{0.8}Co_{0.1}Mn_{0.1}O_2/Li_xCoO_2$ hybrid composite.
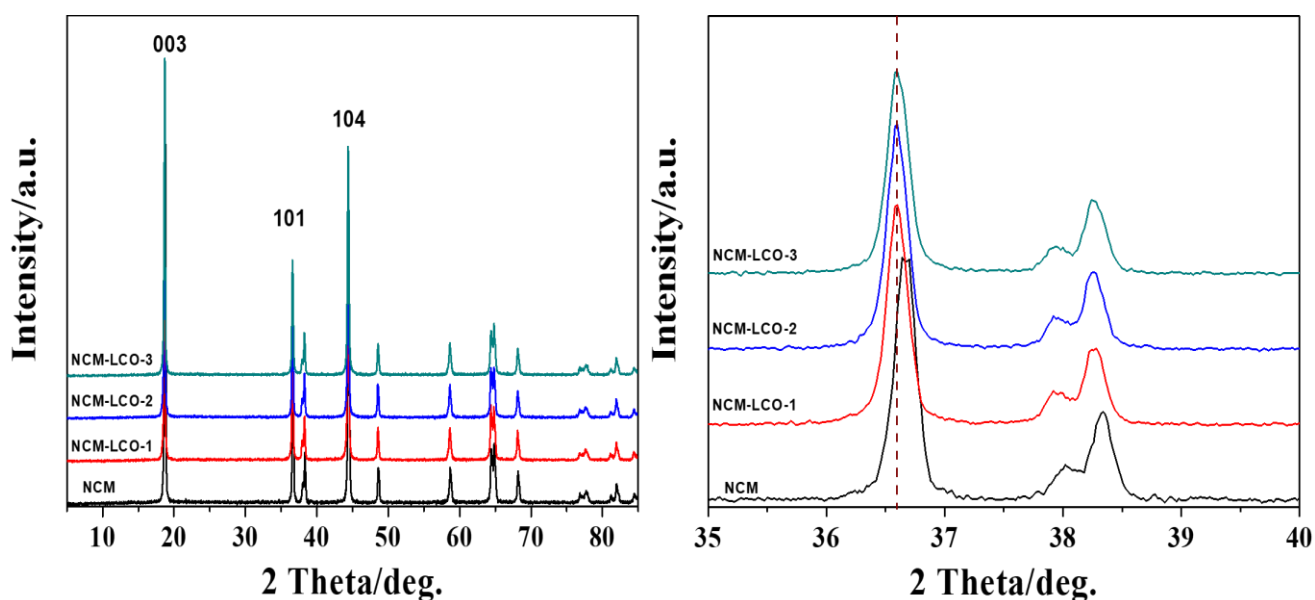

Figure 1. XRD pattern of NCM, NCM-LCO-1, NCM-LCO-2, NCM-LCO-3.

Table 1. Lattice parameters of all samples.

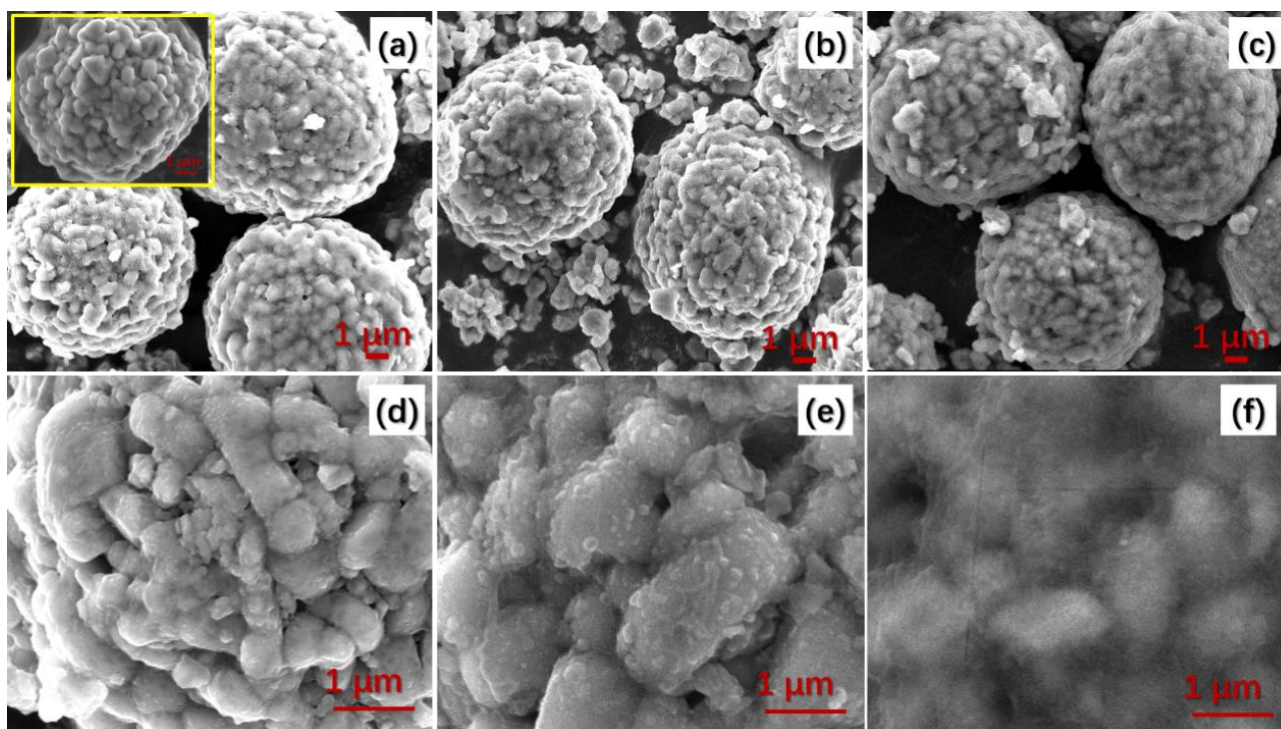| Samples	(003)		(104)		$I_{(003)}/I_{(104)}$	Lattice Parameters	
	2θ(°)	d(Å)	2θ(°)	d(Å)		a(Å)	c(Å)
NCM	18.761	4.7260	44.466	2.0357	1.214	2.87502	14.19711
NCM-LCO-1	18.750	4.7287	44.431	2.0373	1.202	2.87453	14.20158
NCM-LCO-2	18.733	4.7328	44.412	2.0381	1.253	2.87442	14.20797
NCM-LCO-3	18.698	4.7418	44.379	2.0396	1.215	2.87472	14.20657

Figure 2 SEM images of: (a) and (d) NCM-LCO-1; (b) and (e) NCM-LCO-2; (c) and (f) NCM-LCO-3; the insert image in (a) is SEM image of NCM.

TEM tests were carried out to investigate the boundary and inner structure of NCM and NCM-LCO-2. As shown in the insert image in Figure 3(a), a clear surface is detected for NCM sample, suggesting the perfect crystallization[21]. During the storage, the residual lithium on the surface of NCM sphere particle can react with trace H_2O and CO_2 and gradually form the inactive LiOH and Li_2CO_3, which is further confirmed by FTIR (Figure 4). In Figure 4, the existence of O-H and C=O bond can be ascribed to the formation of LiOH and Li_2CO_3. However, with the help of the liquid coating strategy, the relatively poor transmittance of the sample after Li_xCoO_2 coating proves that the side reaction has been alleviated as well. As shown in Figure 3(b) and 3(c), some Li_xCoO_2 phase and interfacial phase are detected. From the HRTEM image in Figure 3(d), the lattice width of 0.45 nm and 0.27 nm correspond to the (111) face and (311) face of layered $LiNi_{0.8}Co_{0.1}Mn_{0.1}O_2$, respectively. Since the coating ratio of Li_xCoO_2 is only 2 wt%, it is hard to detect the crystallinity of Li_xCoO_2 from HRTEM. It is reported that the partly coating can also alleviate the side reaction and improve the electrochemical performance of cathode material in lithium ion batteries[22,23]. Thus, it can be speculated that the Li_xCoO_2 has been successfully coated on the surface of NCM material via the liquid method.

BET tests were conducted to characterize the specific surface area for both NCM and NCM-LCO-2 samples. It can be observed in Figure 5 that all adsorption/desorption curves belong to *III*-type with no inflection point. The pore volume of NCM is 1.513×10^{-3} cm^{-3} g^{-1} while the coated one possesses 8.649×10^{-4} cm^{-3} g^{-1}. The decrease pore volume may attribute to the reduced gap between primary particles contributed from the filling up of the Li_xCoO_2 material.
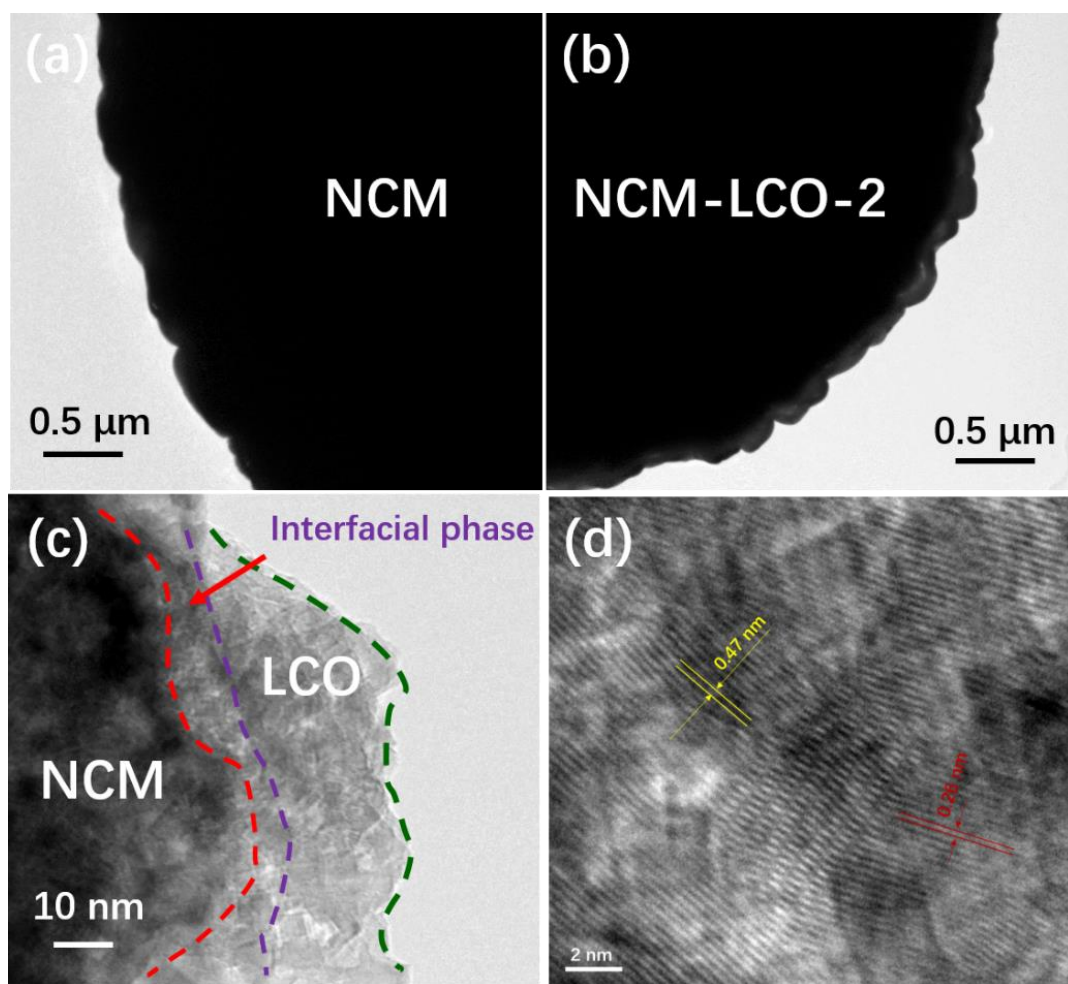
Figure 3 TEM images of (a) NCM and (b) NCM-LCO-2, (c) and (d) high resolution TEM images of NCM-LCO-2.
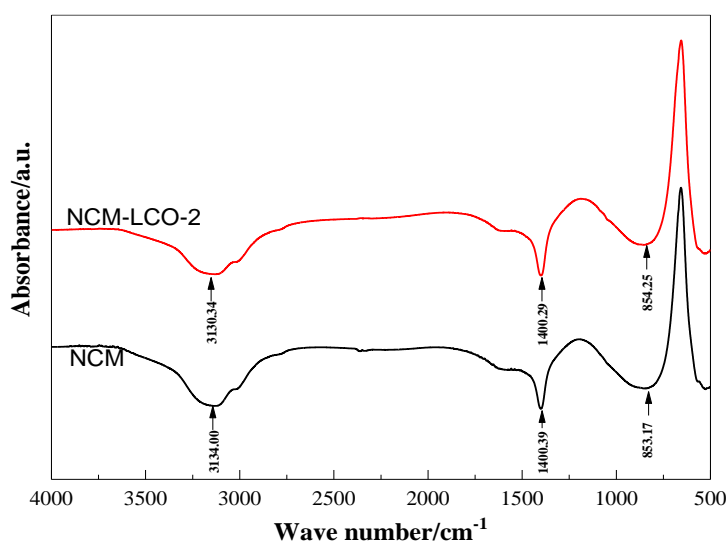

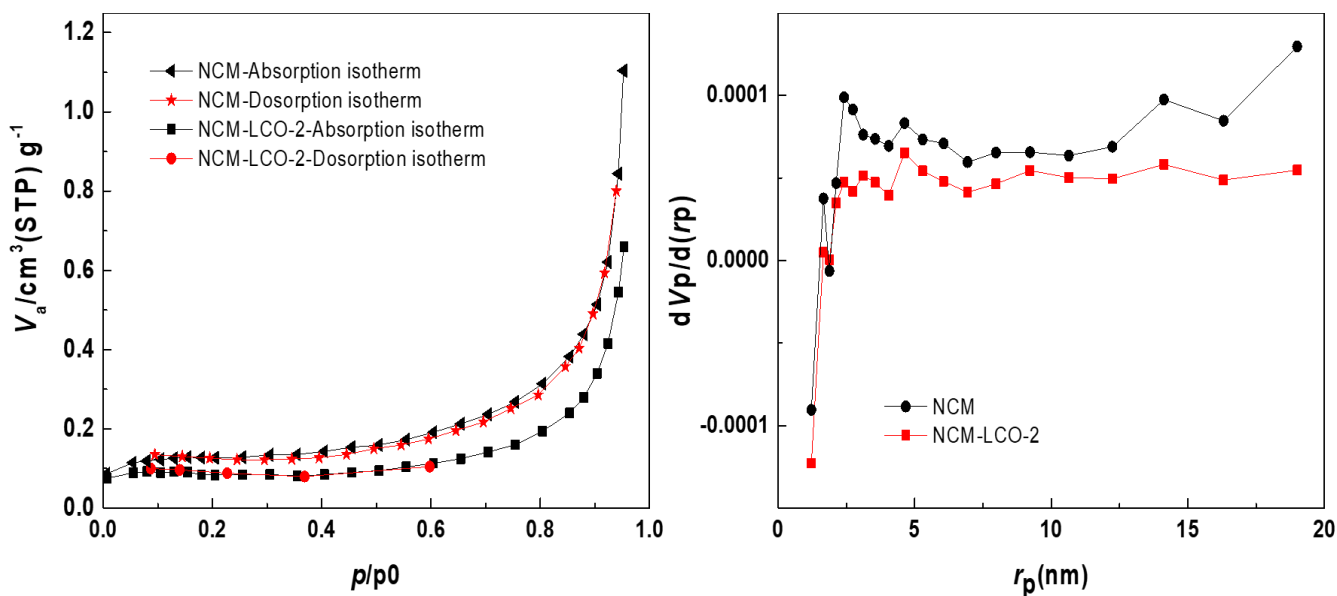**Figure 4.** FTIR results of NCM and NCM-LCO-2.

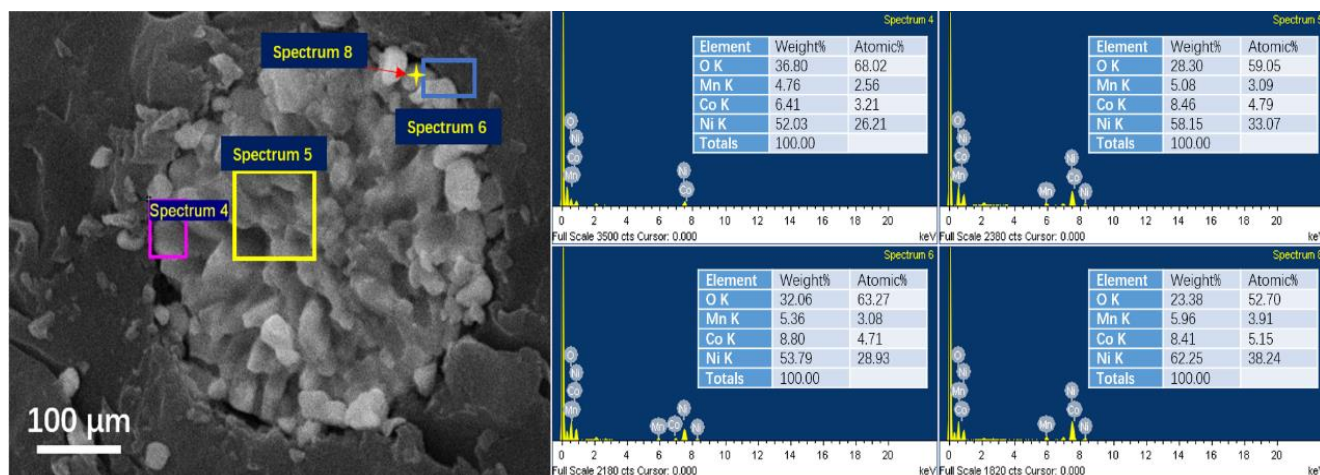**Figure 5.** BET results of NCM and NCM-LCO-2.

Figure 6. SEM-EDS images and different selected spots of NCM-LCO-2.

In order to further investigate the surface element components and their dispersion, we selected SEM-EDS to characterize NCM-LCO-2 sample. From Figure 6, the cobalt is uniformly dispersed on the cross-section of particles with the atom ratio ranging from 3.2 to 5.1%. In comparison, the manganese atom ratio is only around 2.56%-3.91%. The ratio of cobalt element beyond than that of manganese element indicates that the Li_xCoO_2 not only coats on the surface of NCM but also immerses into the inner gap between $LiNi_{0.8}Co_{0.1}Mn_{0.1}O_2$ primary particles.
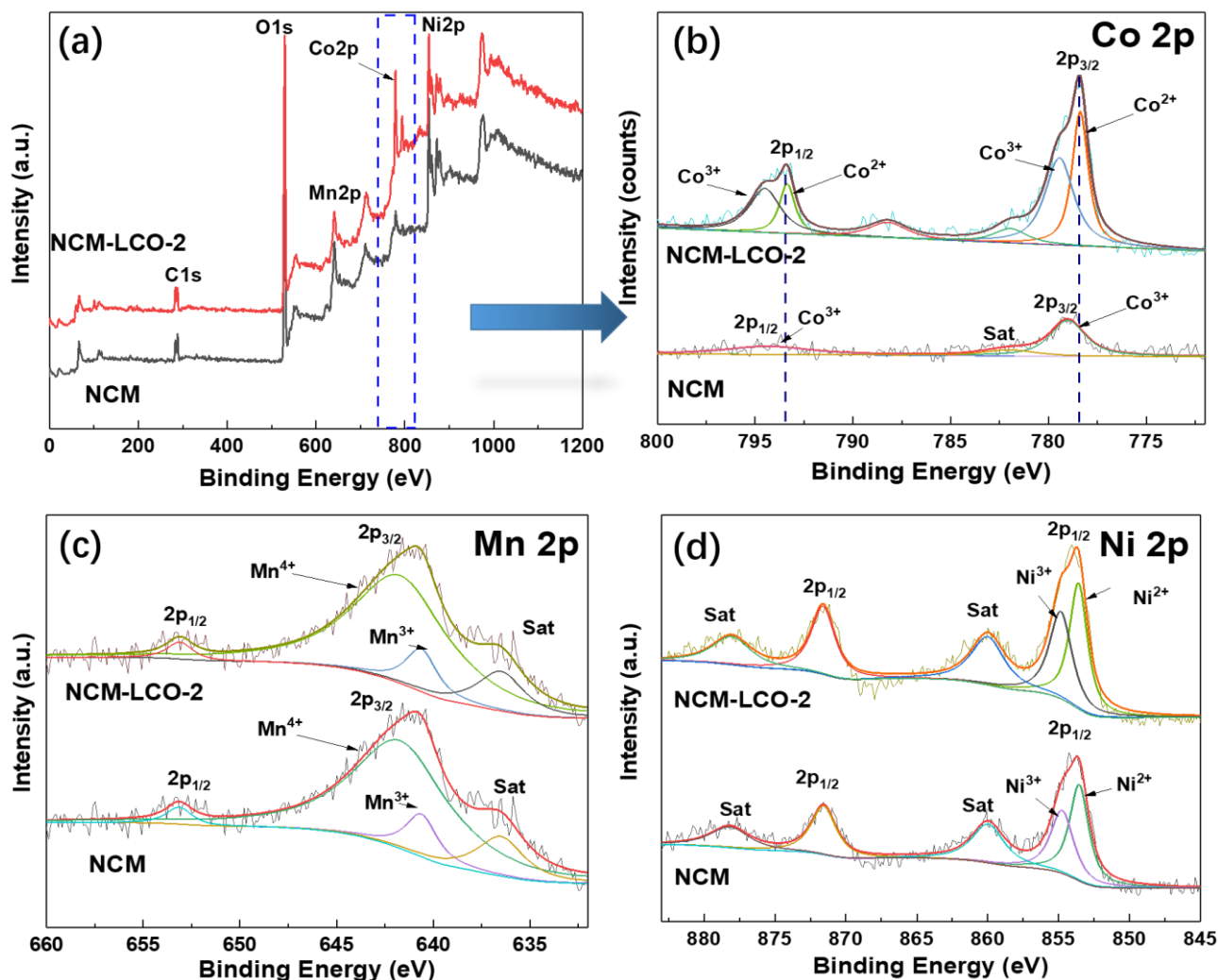
Figure 7. XPS pattern of NCM and NCM-LCO-2: (a) full spectrum; (b) Co spectrum; (c) Mnspectrum and (d) Ni spectrum.

XPS was used to further investigate the surface chemical species and oxidation state of NCM and NCM-LCO-2 sample after cycling. Figure 7(a) gives the full spectra of pristine NCM and NCM-LCO-2. Figure 7(b) shows the high-resolution of Mn2p spectra from the full spectra. The peak at 641.1 eV and 652.9 eV is related to Mn2p$_{3/2}$ and Mn2p$_{1/2}$[24,25], respectively. It demonstrates that the main valance state of Mn is +4. The analysis of Mn2p represents that the chemical environment of Mn does not alter after the Li$_x$CoO$_2$ coating. Figure 7(c) shows the high-resolution of Ni2p spectra, where the peaks of 871.6 eV and 878.1 eV can be attributed to the main peaks and the satellite peaks of Ni 2p$_{1/2}$[26,27]. Additionally, the Ni spectra also has two peaks at 853.6 eV and 854.9 eV, corresponding to Ni^{2+} and Ni^{3+}, respectively. According to the simulated peak area from Ni 2p$_{3/2}$, the ratio between Ni^{2+} and Ni^{3+} is 53.6:46.4 before coating Li$_x$CoO$_2$, while the ratio changes to 56.2:43.8 after the surface coating. Figure 7(d) gives the high-resolution of Co 2p. For the pristine NCM, the Co 2p$_{3/2}$ peak locates at 779.0 eV while the Co 2p$_{1/2}$ peak locates at 794.4 eV, indicating the main valance state of Co is +3. After surface coating with Li$_x$CoO$_2$, the Co 2p$_{3/2}$ peak divides into two peaks at 778.4 eV and 779.4 eV, which can be ascribed to the co-existence of Co^{2+} and Co^{3+}[28].

Simultaneously, the Co $2p_{1/2}$ peaks at 793.4 eV and 794.5 eV illustrate the valance state of cobalt are +2 and +3 with the ratio reaching 35.8: 64.2 after the coating. From above discussion,we can conclude that the main valence of cobalt before the Li_xCoO_2 coating is +3 while it transforms to the mixture state of +2 and +3 after the coating.
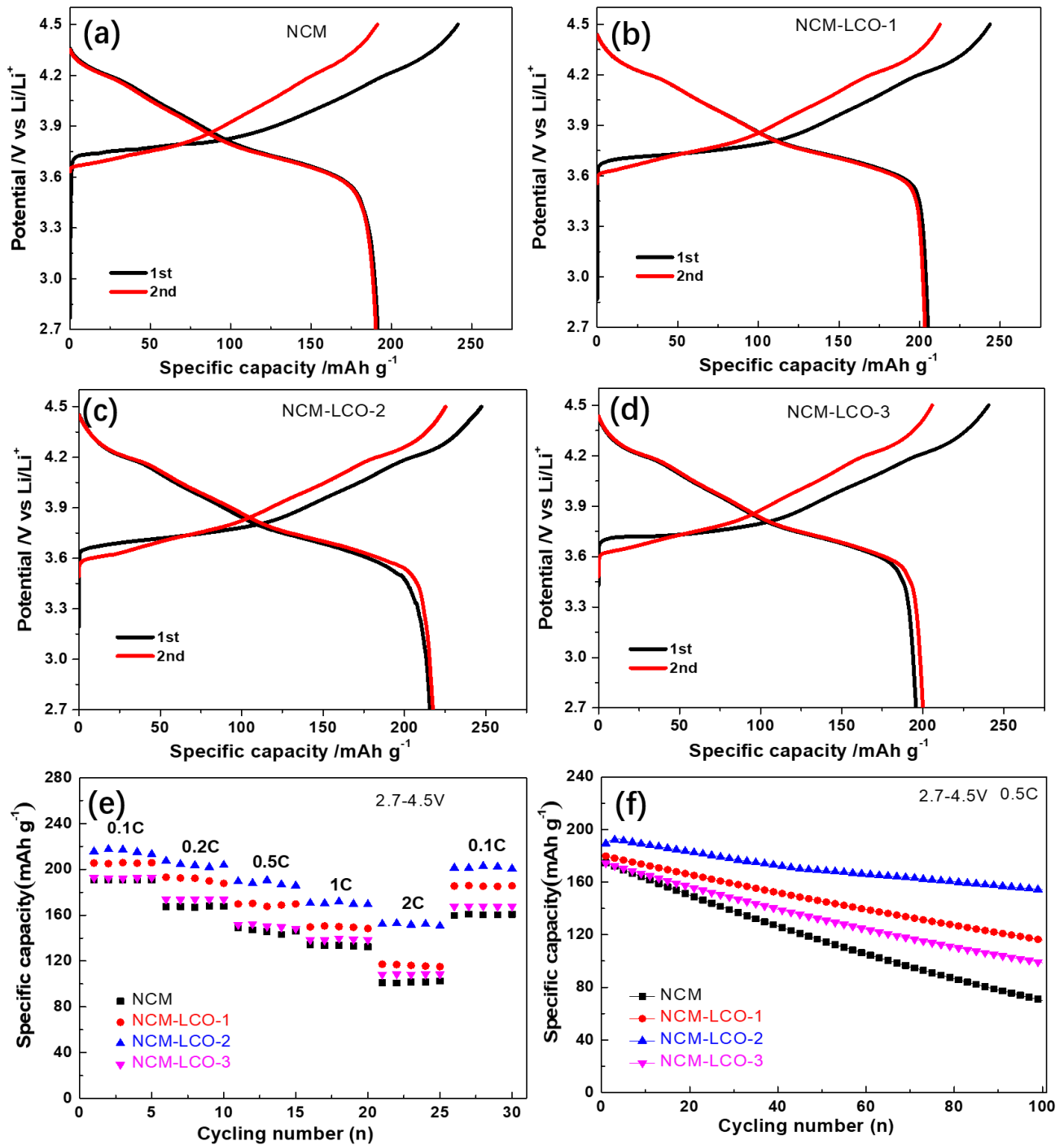

Figure 8. Initial and secondary charge/discharge profiles of (a) NCM; (b) NCM-LCO-1; (c) NCM-LCO-2 and (d) NCM-LCO-3 at 0.1 C rate; (e) rate stability and (f) cycling stability of NCM, NCM-LCO-1, NCM-LCO-2 and NCM-LCO-3.

Figure 8 demonstrates the initial two charge/discharge curves of all samples in the potential range 2.7-4.5 V at 0.1 C. From the Figure, the charging plateau decreases while the discharging plateau increases after Li_xCoO_2 coating, suggesting the reduced polarization and improved cycling reversibility. Interestingly, a new charging plateau appears at 4.25 V, which can be attributed to the increased content of cobalt arising from the stronger electrochemical reaction between Co^{3+}/Co^{4+}. From Table 2, when the charging limit voltage increases to 4.5 V, the specific capacity of NCM increases, while, all other samples possess significant improvement in the first and second columbic efficiency in spite of the slight increase of specific capacity. Among these samples,the first columbic efficiency of NCM-LCO-2 is 87% in comparison to 79% of NCM. Figure 8(e) compares the rate performance of NCM and Li_xCoO_2-coated samples at 0.1- 2 C rates. The rate capability of Li_xCoO_2-coated sample shows significant improvement. Among them, the NCM-LCO-2 sample delivers the superior rate performance with specific capacity of 152.8 mAh g^{-1} in comparison with that of 101.6 mAh g^{-1} of the NCM. After different rate cycling, the NCM-LCO-2 sample delivers 93.9% of capacity recovery ability while the NCM only possesses 84.2%. The surface coating sample with 2 wt%LCO gives much better rate performance than that the uncoated one. The cycling stability of samples are also investigated, as shown in Figure 8(f). From the pattern, all Li_xCoO_2-coated samples show superior cycling stability than that of NCM. Compared with 40.2% of capacity retention for NCM, the NCM-LCO-2 sample maintains 81.5% of capacity retention after 100 cycles at 0.5 C, demonstrating an excellent cycling stability.

Table 2. First and second charge/discharge capacity and corresponding columbic efficiency of all samples.

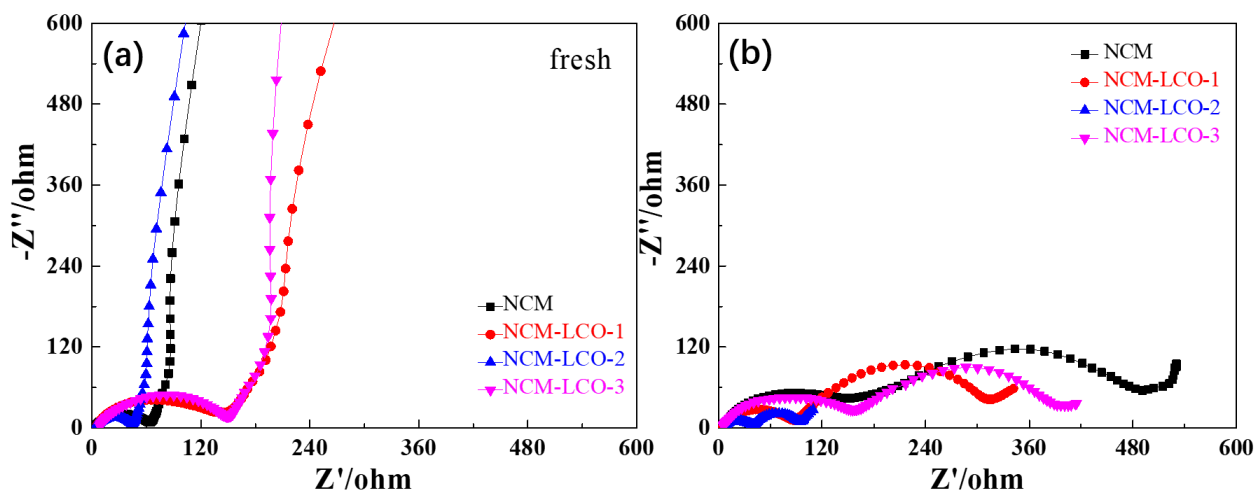| Samples	First charge/discharge capacity (mAh g^{-1})	Columbic efficiency (%)	Second charge/discharge capacity (mAh g^{-1})	Columbic efficiency (%)
NCM	265.1/201.0	69.0%	203.4/200.0	90.0%
NCM-LCO-1	266.4/205.7	77.2%	208.9/201.0	96.2%
NCM-LCO-2	255.4/203.8	79.8%	203.9/205.6	100.8%
NCM-LCO-3	259.0/205.8	79.5%	208.1/207.3	99.6%

Figure 9. EIS pattern of (a) fresh state, and (b) after 100 cycles state of NCM, NCM-LCO-1, NCM-LCO-2 and NCM-LCO-3.

In order to further analyze the reason, EIS tests were carried out before and after the cycling. Figure 9(a) shows the impedance curves before cycling. The curve is composed of a semicircle at high frequency region and a line at low frequency region. Since there is no solid electrolyte interface (SEI) film, the semicircle at high frequency indicates the charge transfer resistance while the line at low frequency represents the solid diffusion of lithium ion among the active material. Figure 9(b) shows EIS pattern of the sample after 100 cycles at the charging state to 4.5 V. The curve also consists of two semicircles at high/middle frequency and a line at low frequency. The first semicircle at high frequency represents the SEI film impedance arising from the diffusion of lithium ion across the SEI film while the second semicircle at middle frequency represents the charge transfer resistance. The line at low frequency stands for the diffusion process of lithium ion among active material[29,30]. Comparison with the results in both patterns, we can conclude that the charge transfer resistance of Li_xCoO_2-coated sample is much smaller than that of NCM. Among all samples, the NCM-LCO-2 sample possesses the smallest charge transfer resistance, which may be the main reason for the improved cycling stability. The existence of surface coating Li_xCoO_2 can prevent the direct contact between NCM and the residual hydrogen fluoride (HF) in electrolyte. The side reaction, especially the corrosion of HF to NCM[31,32], can be effectively impeded and the cycling stability of the material can be improved.
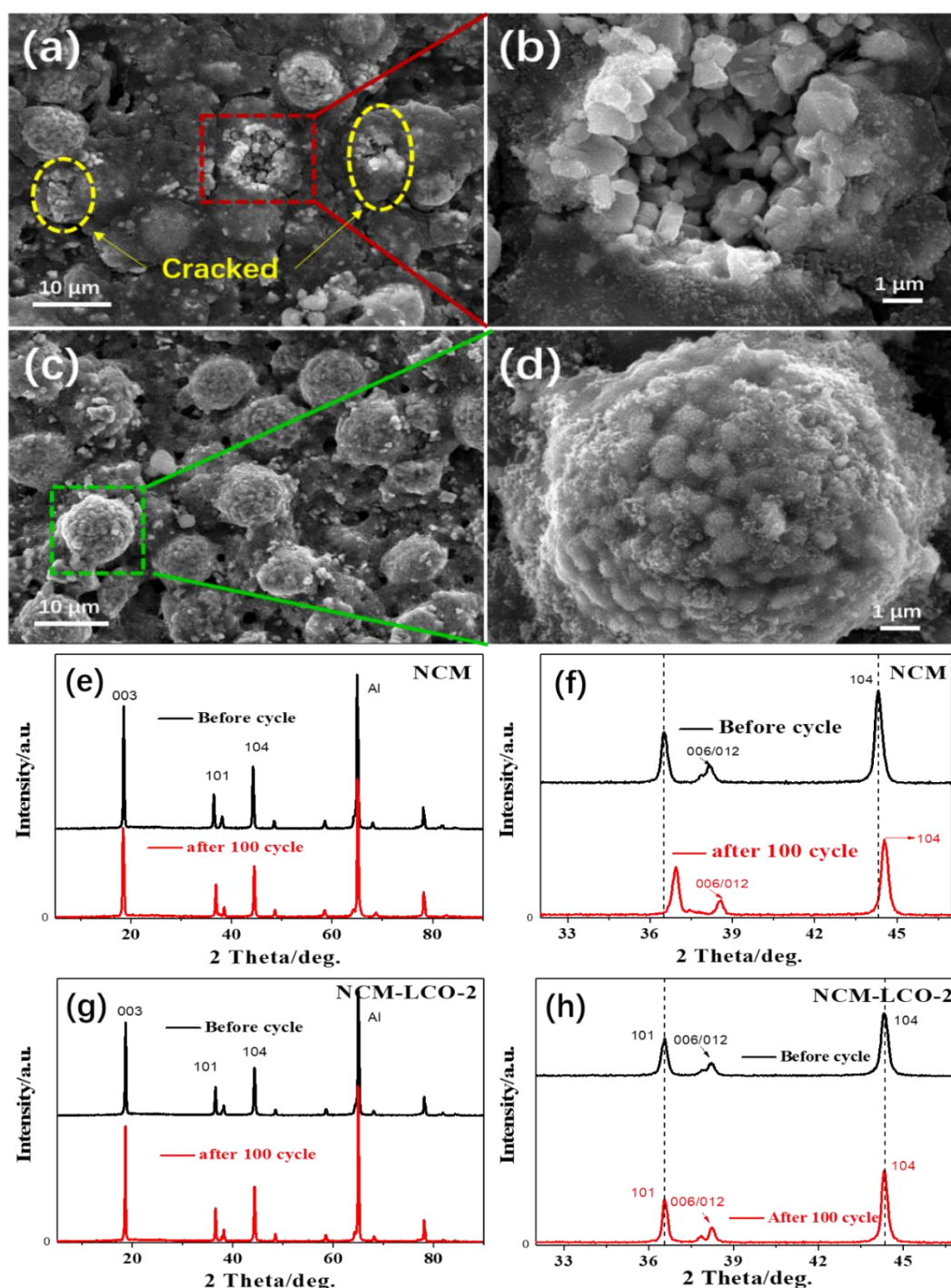
Figure 10. SEM images of NCM electrode (a-b) after 100 cycle; and NCM-LCO-2 electrode(c-d) after 100 cycle. And corresponding XRD pattern of NCM electrode (e) before and after 100 cycle, (f) enlarged range; and NCM-LCO-2 electrode (g) before and after 100 cycle, (h) enlarged range.

In order to deeply investigate the improved electrochemical properties, the morphology and crystal alteration after the cycling have been carried out. SEM images of NCM electrode and NCM-LCO-2 electrode are shown in Figure 10(a-d). For NCM-LCO-2 sample, there is no obviously morphological alteration of the electrode after cycling. However, for NCM, there are detectable surface cracks after cycling. This phenomenon confirms that the Li_xCoO_2 coating can effectively impede the direct contact of NCM with HF in electrolyte, alleviate the element dissolution, and improve the stability

of surface architecture. Additionally, the inner coating layer can also compact the $LiNi_{0.8}Co_{0.1}Mn_{0.1}O_2$ primary particle, reduce the trace crack and prevent the formation of new SEI film. As we known, the formation of SEI film can produce additional resistance between crystal interface and is adverse to the electrochemical properties[33]. Simultaneously, the XRD pattern of samples before/after cycling is shown in Figure 10(e-h). From the pattern, the diffraction peaks shift to higher 2θ angle after cycling, indicating the irreversibility of crystal structure and the broken of layer architecture. For NCM sample, the peaks of (006) and (012) are individual before cycling. However, the pair peaks combine into one broad peak after cycling, indicating the broken of layer architecture during cycling. For coated sample, there is no obvious shift for all diffraction peaks and the separated peaks of (006) and (012) still exist, demonstrating that the layer structure does not been broken during cycling. The maintenance of layer structure is one of the reasons for the improved cycling performance.

Figure 11(a) and 11(b) compare the CV curves of NCM and NCM-LCO-2 samples before/after cycling. For NCM, the 1st cycle shows a significant peak at 4.1 V during oxidation process, which can be attributed to the activation and the formation of SEI film. While there is another oxidation peaks at 3.7 V for the second and third cycle. For the NCM-LCO-2 sample, the 1st cycle shows an oxidation peak at 3.918 V and a corresponding reduction peak is observed at 3.7 V. The potential gap between oxidation peak and reduction peaks is only 0.218 V, while the gap value reaches 0.316 V for the NCM sample. It is well known that the higher potential gap of CV, the lower electrochemical reversibility of the battery. Thus, we further confirm that the electrochemical process becomes more reversible after the Li_xCoO_2 coating.

Table 2. Comparison of electrochemical properties of hybrid cathode material.

| Samples	Initial discharge capacity （mAh g^{-1}）	Columbic efficiency （%）	Rate performance	Ref.
rGO@LiNi$_{0.6}$Co$_{0.2}$Mn$_{0.2}$O$_2$	196.5	87.6	≈150 mAh g^{-1} at 500 mA g^{-1}	[34]
LiAlO$_2$@LiNi$_{0.6}$Co$_{0.2}$Mn$_{0.2}$O$_2$	202.8	≈79.5	≈165 mAh g^{-1} at 362 mA g^{-1}	[35]
NSC@LiNi$_{0.8}$Co$_{0.1}$Mn$_{0.1}$O$_2$	202.12	≈91.8	111.39 at 550 mA g^{-1}	[36]
Li$_2$O-$_2$B$_2$O$_3$@ iNi$_{0.8}$Co$_{0.1}$Mn$_{0.1}$O$_2$	193.1	90.06	–	[37]
LaPO$_4$@LiNi$_{0.5}$Co$_{0.2}$Mn$_{0.3}$O$_2$	147.8	92.89	111.39 at 360 mA g^{-1}	[38]
LiNi$_{0.8}$Co$_{0.1}$Mn$_{0.1}$O$_2$/ Li$_x$CoO$_2$	203.8	79.8	≈160 mAh g^{-1} at 550 mA g^{-1}	Our work
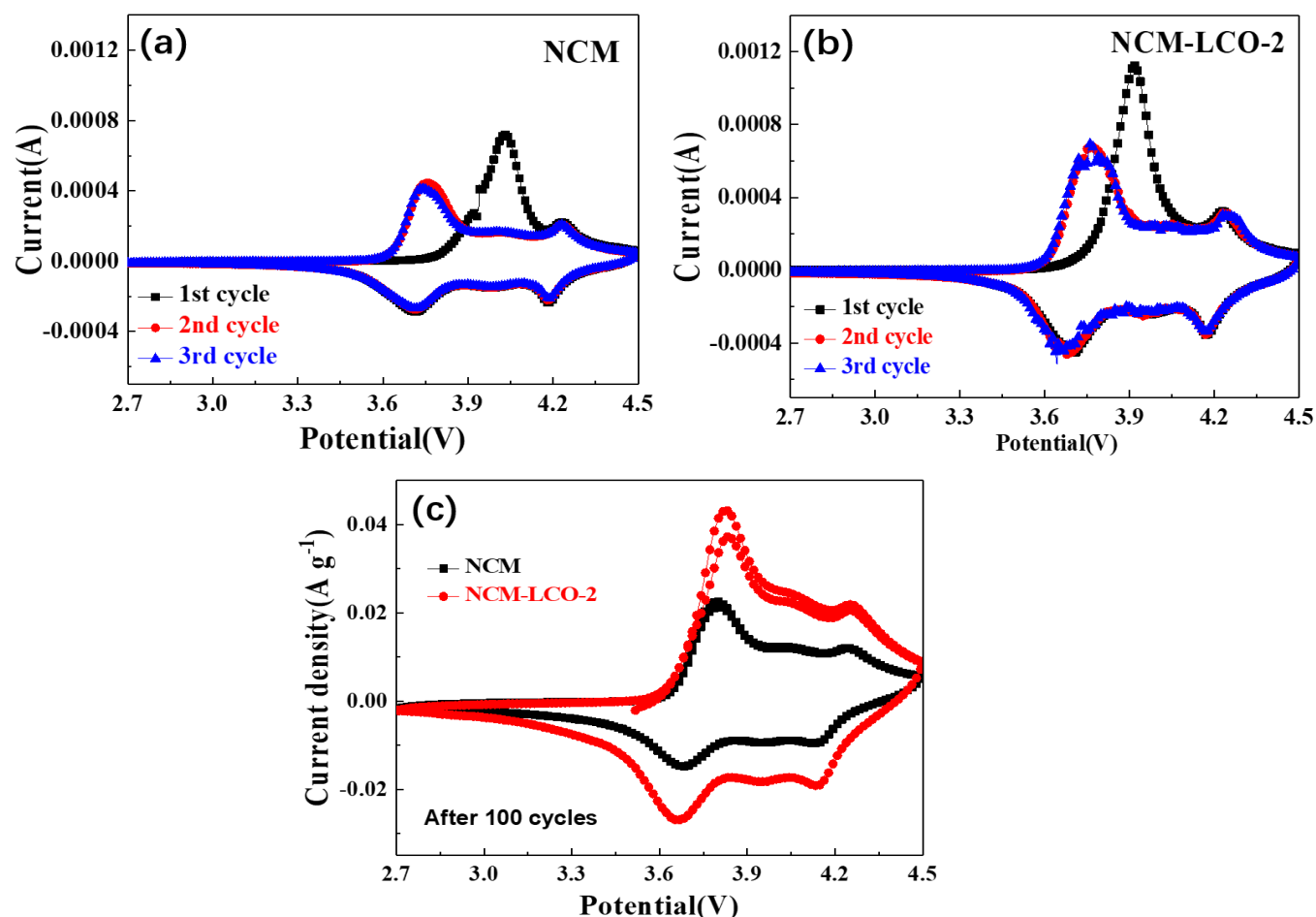
Figure 11. CV curves of (a) NCM, (b) NCM-LCO-2, and (c) comparison of both electrodes after 100 cycle.

Figure 11(c) further compares the CV curves of NCM and NCM-LCO-2 sample after 100 cycles. From the Figure, the peak current density for the oxidation/reduction behavior of NCM-LCO-2 is much higher than that of NCM. Since the covered area from CV curves proportionally corresponds to the specific capacity, the NCM-LCO-2 delivers higher capacity than that of NCM after 100 cycling, which keeps consistent with previous conclusion that the surface coating can effectively improve the cycling stability and maintain higher specific capacity than bare sample

Table 2 further shows the compariosn of electrochemical properties between our material and the similar hybrid cathode material in lithium ion battery. Obviously, Our material has certain advantage or is compariable with other hybrid materials under the similar condition of initial discharge capacity, columbic efficiency or high discharge rate.

4. CONCLUSIONS

Core-shell like $LiNi_{0.8}Co_{0.1}Mn_{0.1}O_2/Li_xCoO_2$ hybrid cathode has been synthesized by a liquid method. After surface coating with Li_xCoO_2, the layer structure of $LiNi_{0.8}Co_{0.1}Mn_{0.1}O_2$ can be well maintained without showing significant particle crack. The direct contact between the electroactive material and HF from electrolyte is alleviated and the formed fuzzy surface

benefits the bridging effect between primary particles to reduce electronic resistance. The chemical attack from OH^- and CO_2 can also be alleviated after Li_xCoO_2 coating. Simultaneously, the liquid penetration strategy is helpful to prevent the formation of SEI film on the surface of primary particle. Benefiting from above reasons, the $LiNi_{0.8}Co_{0.1}Mn_{0.1}O_2/Li_xCoO_2$ hybrid cathode exhibits excellent electrochemical capability, superior cycling stability and improved rate performance, showing a promising advantage in lithium ion batteries.

CONFLICTS OF INTEREST
There are no conflicts to declare.

References

1. J. H. Song, K. Wang and J. M. Zheng, *ACS Energy Lett.*, 5(2020)1718.
2. T. Kim, W. Song, D. Y. Son, L. K. Ono and Y. Qi, *J. Mater. Chem. A*, 7(2019) 2942.
3. S. Gao, X. Zhan and Y. T. Cheng, *J. Power Sources*, 410(2019)45.
4. E. Matthias, M. Winter and F. M. Schappacher, *J. Power Sources*, 397(2018) 68.
5. H. Shuai, J. Li and W. Hong, *Small Methods*, 3(2019)5.
6. U. Kim, H. Ryu and J. Kim, *Adv. Energy Mater.* 9(2019)15.
7. S. Y. Park, W. J. Baek and Lee S Y, *Nano Energy*, 49(2018)1.
8. Y. P. Fu, Y. Q. He and Y. Yang, *J. Alloys Compd.*, 832(2020)154920.
9. H. J., W. Park and J. Holder, *J. Nanosci. Nanotechnol.*, 20(2020)6005.
10. R. J. Wang, J. Y. Zheng and X. M. Feng, *J. Solid State Electrochem.*, 24(2020)511.
11. C. Hao, X. Li and C. Han, *Electrochim. Acta*, 344(2020)136142.
12. L. Chen, X. Chen and Y. Q. Wen, *J. Nanosci. Nanotechnol.*, 20(2020)4854.
13. T. Sattar, S. Lee and S. Sim, *Int. J. Hydrogen Energy*, 45(2020)19567.
14. P. Yan, J. Zheng and L. Jian, *Nat. Energy*, 3(2018)600.
15. N. D. Phillip, B. L. Armstrong, L. Beth and C. Daniel, *ACS Omega*, 5(2020)14968.
16. D. W. Zhang, Y. J. Li and X. M. Xi, *Sustainable Energy Fuels*, 4(2020)3352.
17. G. Y. Ding, Y. H. Li and Y. Gao, *ACS Sustainable Chem. Eng.*, 8(2020)9632.
18. Y. Bai, K. J. Zhao and Y. Liu, *Scr. Mater.*, 183(2020)45.
19. Z. Chen, D. L. Chao and M. H. Chen, *RSC Adv.*, 10(2020)18776.
20. K. Sahni, M. Ashuri and Q. R. He, *Electrochim. Acta*, 301(2019)8.
21. M. K. Shobana, *J. Alloys Compd.*, 802(2019)477.
22. P. P. Pang, Z. Wang and Y. M. Deng, *ACS Appl. Mater. Interfaces*, 12(2020)27339.
23. L. Y. Yang, K. Yang and J. X. Zheng, *Chem. Soc. Rev.*, 49(2020)4667.
24. B. J. Tan, K. J. Klabunde and P. M. A. Sherwood, *J. Am. Chem. Soc.*, 3(1991)855.
25. B. Aktekin, F. Massel and M. Ahmadi, *ACS Appl. Energy Mater.*, 3(2020)6001.
26. R. S. Negi, S. P, Culver and A. Mazilkin, *ACS Appl. Mater. Interfaces*, 12(2020)31392.
27. Y. Q. Cui, C. Y. Zhu and R. Huang, *Int. J. Electrochem. Sci.*, 15(2020)5440.
28. H. Park, S. Jo and T. Song, *Crystal Growth & Design*, 20(2020)4749.

29. T. Toma, R. Mazezono and K. Hongo, *ACS Appl. Energy Mate.*, 3(2020)4078.
30. H. Jung, W. Park and J. Holder, *J. Nanosci. Nanotechnol.*, 20(2020)6505.
31. Y. G. Zou, Y. B. Shen and Y. Q. Wu, *Chem. Eur. J.*, 26(202)7930.
32. W. R. Li, H. Zhuang and L. J. Guo, *J. Mater. Sci.-Mater. Electron.*, 31(2020)11141.
33. S. Y. Deng, Y. J. Li and Q. Y. Dai, *Sustainable Energy Fuels*, 3(2019)3234.
34. W. Ahn, M. H. Seo and T. K. Pham, *Front. Chem.*, 7(2019)361.
35. Z. L. Xiao, C. M. Hu, L. B. Song and L. J. Li, *Ionics*, 24(2018)91.
36. M. Nathagopal, P. Santhoshkumar and N. Shaji, *Appl. Surf. Sci.*, 511(2020)145580.
37. H. Zhang, H. Zhao and J. Xu, *Int. J. Green Energy*, 17(2020)447.
38. X. D. Jiang, Z. T. Yuan, J. X. Liu and X. Jin, *Int. J. Electrochem. Sci.*, 13(2018)2341.